(Un)Explained EMIC Waves: Understanding Quiet Time EMIC Wave Drivers

Remya, B.; Halford, A. J.; Noh, Sung Jun; Fernandes, Philip A.; Grison, B.; Wang, D.; Himmelsback, J.; Esman, T.; Graham, D.B.; Sibeck, D.G.; Raita, T.; Dimri, A.P.

To be published in: Journal of Geophysical Research: Space Physics

DOI to publisher's version: 10.1029/2024JA033125

(Un)Explained EMIC Waves: Understanding Quiet Time EMIC Wave Drivers

B. Remya[1], A.J. Halford[2], S. J. Noh[3], P. A. Fernandes[3], B. Grison[4], D. Wang[5], J. Himmelsbach[5], T. Esman[2], D. B. Graham[6], D.G. Sibeck[2], T. Raita[7], A. P. Dimri[1]

[1]Indian Institute of Geomagnetism, Navi Mumbai, India.
[2]NASA Goddard Space Flight Center, Maryland, USA.
[3]Los Alamos National Laboratory, New Mexico, USA.
[4]Department of Space Physics, Institute of Atmospheric Physics CAS, Prague, Czechia.
[5]GFZ Potsdam, Germany.
[6]Swedish Institute of Space Physics (IRF), Uppsala, Sweden.
[7]Sodankylä Geophysical Observatory, University of Oulu, Finland.

Key Points:

- A portion of EMIC waves are observed during extremely quiet solar wind and geomagnetic conditions without observations of common drivers.
- Substorm injections of 10-15 keV protons take hours to drift in MLT and generate EMIC waves long after the typically used substorm period.
- Marginal enhancement in dynamic pressure/ion flux is sufficient to trigger EMIC waves under such extremely quiet geomagnetic conditions.

Corresponding author: Remya Bhanu, remyaphysics@gmail.com

Abstract

Electromagnetic ion cyclotron (EMIC) waves are known to be generated through cyclotron resonance with the local ion particle population and grow when there is a large enough temperature anisotropy. In general, these temperature anisotropies necessary for wave growth are found to be associated with either solar wind pressure pulses or particle injections during geomagnetic storms or substorms. However, some EMIC events do not show any clear association with these known drivers and appear unexplained. In our analysis of high-amplitude (>1 nT) non-storm time EMIC waves, we find that 24 out of the 223 (∼11%) EMIC events with peak amplitude greater than 1 nT were not found to be associated with any clear EMIC wave driver. This raises a compelling question: What magnetospheric or solar wind driver provides the free energy to grow these quiet-time EMIC waves? Here, we examine two EMIC events on 13 April 2017 and 13 February 2014, which were excited during extremely quiet solar wind and geomagnetic conditions. An in-depth analysis of field and particle measurements from multiple datasets, including ground and in-situ data for these two events, indicates that extremely weak and otherwise insignificant pressure values and/or very weak substorm injections occurring multiple hours before the event play a significant role in quiet time wave generation.

Plain Language Summary

Electromagnetic cyclotron (EMIC) waves can be found in Earth's magnetosphere. Here, these waves can then impact the space environment by causing the loss of radiation belt electrons and ring current protons. The loss of energetic particles impacts the environment of satellites, as well as the dynamics in the middle atmosphere chemistry where these particles ultimately are lost. Understanding when these waves are occurring and, thus, when we expect to see these impacts is important. Typically, EMIC waves are associated with pressure pulses from the solar wind and/or geomagnetic storms or substorms. However, ∼11% of high amplitude, non-storm time EMIC waves are not associated with these known drivers. Within this paper, we look closely at two quiet time events and provide new insight into what drives this portion of the waves.

1 Introduction

Electromagnetic ion cyclotron (EMIC) waves observed in Earth's inner magnetosphere fall in the 0.15 Hz Pc1-2 frequency range and can play a vital role in the loss process of both ring current protons and radiation belt electrons (e.g., Jordanova et al., 2008; Thorne & Kennel, 1971). Hence, understanding EMIC wave drivers and generation mechanisms is essential for understanding magnetospheric dynamics. EMIC waves are understood to be triggered by an increase of temperature anisotropy $T_\perp/T_\parallel > 1$ in the $\sim 10 - 100$ keV energy proton population of the magnetosphere (Gary, 1992). The general scenario for such instability condition occurs during the injection of protons from the nightside owing to geomagnetic storms or substorms (e.g., Cornwall & Schulz, 1971; Vasyliunas, 1975; Blum et al., 2015; Remya et al., 2018, 2020) or during the compression of the dayside magnetosphere due to interplanetary shocks or solar wind pressure pulses (e.g., Olson & Lee, 1983; Anderson & Hamilton, 1993). The temperature anisotropy of the hot protons is known to provide the free energy for these waves to grow. The growth of the EMIC waves is further controlled by other environmental factors, such as the local cold and hot ion density, ion composition (Young et al., 1981; Rauch & Roux, 1982; Gary, 1992; Allen et al., 2016) and minimum magnetic field conditions where the wave vector is parallel and minimum along the magnetic field (Kozyra et al., 1984; Loto'aniu et al., 2005).

EMIC waves in the Earth's magnetosphere are commonly observed with frequencies below the proton gyrofrequencies (Ω_{H^+}) at their source region. Additionally, due to the presence of multiple ion species (i.e., Hydrogen, Helium and Oxygen), EMIC waves occur in three distinct emission bands separated by their corresponding ion gyrofrequencies: hydro-

gen band (H^+ band), helium band (He^+ band), and oxygen band (O^+ band). After their generation in the equatorial source latitudes, EMIC waves propagate along the magnetic field lines to the ionosphere, get trapped in ionospheric ducts, and further propagate to ground where they can be detected as geomagnetic pulsations in the Pc12 frequency range (Johnson & Cheng, 1999). EMIC waves observed on the ground can have major characteristic changes from their magnetospheric counterpart, including polarization, wave power, and wave normal angle, due to the effects of propagation in the ionospheric waveguide (e.g., Arnoldy et al., 1979; Fraser & Nguyen, 2001).

EMIC waves occur throughout the Earth's inner and outer magnetosphere, covering all L-shells and Magnetic Local Time (MLT) sectors. However, their highest occurrence probability is observed to be in the dusk (afternoon) sector (e.g., Erlandson & Ukhorskiy, 2001; Halford et al., 2010; Keika et al., 2013; Wang et al., 2015; Allen et al., 2015; Halford et al., 2016; Remya et al., 2023) when the enhanced convection during storms and large substorms inject hot protons from the nightside magnetotail, which then drift duskward due to the gradient and curvature of the Earth's magnetic field. These hot protons overlap with the preexisting cold ions, making the wave unstable by reducing the instability threshold. A second peak in the occurrence rate is on the dayside (noon sector), predominantly at higher L-shells (e.g., Anderson et al., 1992b; Usanova et al., 2012) or closer to the magnetopause (e.g., Grison et al., 2021), which are understood to be associated with the compression of the dayside magnetosphere during solar wind dynamic pressure pulses (e.g., Usanova et al., 2008; McCollough et al., 2012; Remya et al., 2015; Engebretson et al., 2015).

In the absence of geomagnetic storms, the major drivers of non-storm time EMIC waves are understood to be injections during substorms (Remya et al., 2020) or sudden dynamic pressure enhancements (Park et al., 2016). However, there is a portion of quiet time EMIC events that are observed isolated, with no clear evidence of magnetospheric compressions or injections. In this paper, we'll look at a subset of large amplitude (> 1 nT) EMIC waves from the Van Allen Probes era (September 2012 to July 2019) where SuperMag identified no substorm activity within the prior 90 minutes, no geomagnetic storm was present or recovering, and no clear pressure pulse could be confidently identified within the solar wind. To put the observations into context, we show two EMIC wave event intervals as representative cases where solar wind and other available particle observations show no clear signatures of any drivers generally known to trigger EMIC waves. We further investigate the possible drivers for these events utilizing multiple in-situ and ground datasets to understand what could have possibly driven these EMIC wave events under such extremely quiet magnetospheric conditions.

2 Data and Methodology

Van Allen Probes mission (Mauk et al., 2013) had twin spacecraft A and B (subsequently referred to as RBSP-A and RBSP-B, respectively) with identical instruments and near identical elliptical orbits. The spacecraft precessed in low inclination ($\sim 10°$) with an apogee of $5.8R_E$ and a perigee of $\sim 1.1R_E$. The high-resolution (64 samples/s) magnetic field data from the Electric and Magnetic Field Instrument Suite and Integrated Science (EMFISIS) tri-axial fluxgate magnetometer (Kletzing et al., 2013) from RBSP-A and RBSP-B are used to identify EMIC waves in this study. The energetic ions in the magnetosphere are measured by the Energetic Particle, Composition, and Thermal Plasma (ECT) suite (Spence et al., 2013) where ions of energies 1 eV to $\sim$52 keV are measured by the ECT/HOPE (Helium Oxygen Proton Electron) mass spectrometer instrument (Funsten et al., 2013) and 50 keV to >1 MeV are measured by the ECT/MagEIS (Magnetic Electron Ion Spectrometer) instrument (Blake et al., 2013). The proton flux data in the energy range from 37 to 488 keV is used from the ECT/RBSPICE (Radiation Belt Storm Probes Ion Composition Experiment) instrument (Mitchell et al., 2013). In particular, the MagEIS data are used only to check for high-energy ion injection signatures during the events, while HOPE and RBSPICE measurements are utilized in calculating the anisotropy parameter described later

in section 3.1 in detail. The location information of EMIC wave observations used in this study, in terms of L-shell, MLT, and MLAT, is obtained from the MagEIS dataset.

Ground signatures of EMIC waves are obtained from the high-resolution magnetic field data from Induction (Search) Coil Magnetometers (ICM) installed at various ground network stations. For the events in this study, we specifically use ICM data from Indian Antarctic station Maitri, Finnish Pulsation magnetometer network stations, ICM array of CARISMA (Canadian Array for Realtime Investigations of Magnetic Activity) network stations (Mann et al., 2008), and ISEE ground magnetometer network stations (Shiokawa et al., 2010). The ground station locations and the satellite footpoints for each event are provided in Figure S1, and the details are listed in Tables S1 and S2 in the Supporting Information (SI).

The particle data measurements from the Cluster mission are obtained from the PEACE instrument for electrons (Johnstone et al., 1997) and CIS/CODIF instrument for protons (Rème et al., 2001). The magnetic field measurements are from the FGM instrument (Balogh et al., 2001). The magnetic field and particle data onboard Geostationary Operational Environmental Satellite (GOES) (Singer et al., 1996) and Los Alamos National Laboratory (LANL) satellite (Reeves et al., 1996) are used to identify and characterize the substorm injection signatures at geosynchronous orbit. The solar wind parameters and geomagnetic indices are obtained from the NASA OMNI database, propagated to the nose of the bow shock. The SME index is obtained from the SuperMAG database (Newell & Gjerloev, 2011a).

We examine EMIC wave events observed by both RBSP-A and RBSP-B during September 2012 to July 2019 ($\sim$7 years). EMIC wave events with $L > 2$ are identified using an automated wave detection algorithm primarily based on Bortnik et al. (2007). The dynamic spectra of 64Hz vector magnetic field measurements are processed in 1 hr intervals, and a wave event is cataloged if its power content is 1 order of magnitude greater than the background noise level. Wave events are at least 4 minutes long, and any two adjacent wave events are to be spaced at least 3 minutes apart to be identified separately. An initial EMIC wave event list thus identified by Remya et al. (2023) is utilized in this study. We then omit all the storm time EMIC waves from this list and utilize only the non-storm time EMIC events for further analysis. Detailed wave and storm identification methods and general occurrence characteristics of EMIC waves are given in Remya et al. (2023).

3 Results and Discussion

The EMIC wave event list consists of 2,442 wave events, out of which the non-storm time EMIC waves comprise $\sim$48% (amounting to 14472 minutes of wave activity). We analyze a subset of these non-storm time EMIC waves, which have their peak amplitudes > 1 nT, to understand the drivers of such large amplitude quiet-time waves. This resulted in a total of 223 wave events, which is less than 10% of the entire EMIC wave list used in Remya et al. (2023). Further, we identify wave drivers associated with these 223 large-amplitude, non-storm time EMIC waves. We particularly look for substorm/injection signatures (AE>100 nT) and/or solar wind dynamic pressure enhancements (>3 nPa) within 90 minutes of the wave onset and associate the wave with that particular driver. In this analysis, we found that out of the 223 EMIC wave events, 66 events were associated with nightside injections during isolated substorm events, 8 events were due to the compression of the magnetosphere due to solar wind pressure pulses, 125 showed association with both isolated substorm injections as well as pressure enhancements, making it difficult to identify the exact driver. The remaining 24 out of 223 (11%) large amplitude, non-storm time EMIC events were not found to be associated with any clear and coincident EMIC wave driver (injection from a substorm or an increase in the temperature anisotropy from a pressure pulse). Within this paper, we consider two prominent events of this subset of larger amplitude (> 1 nT) quiet-time EMIC waves in order to determine what drivers were present and were able to generate such large amplitude EMIC waves in an otherwise quiet magnetosphere.

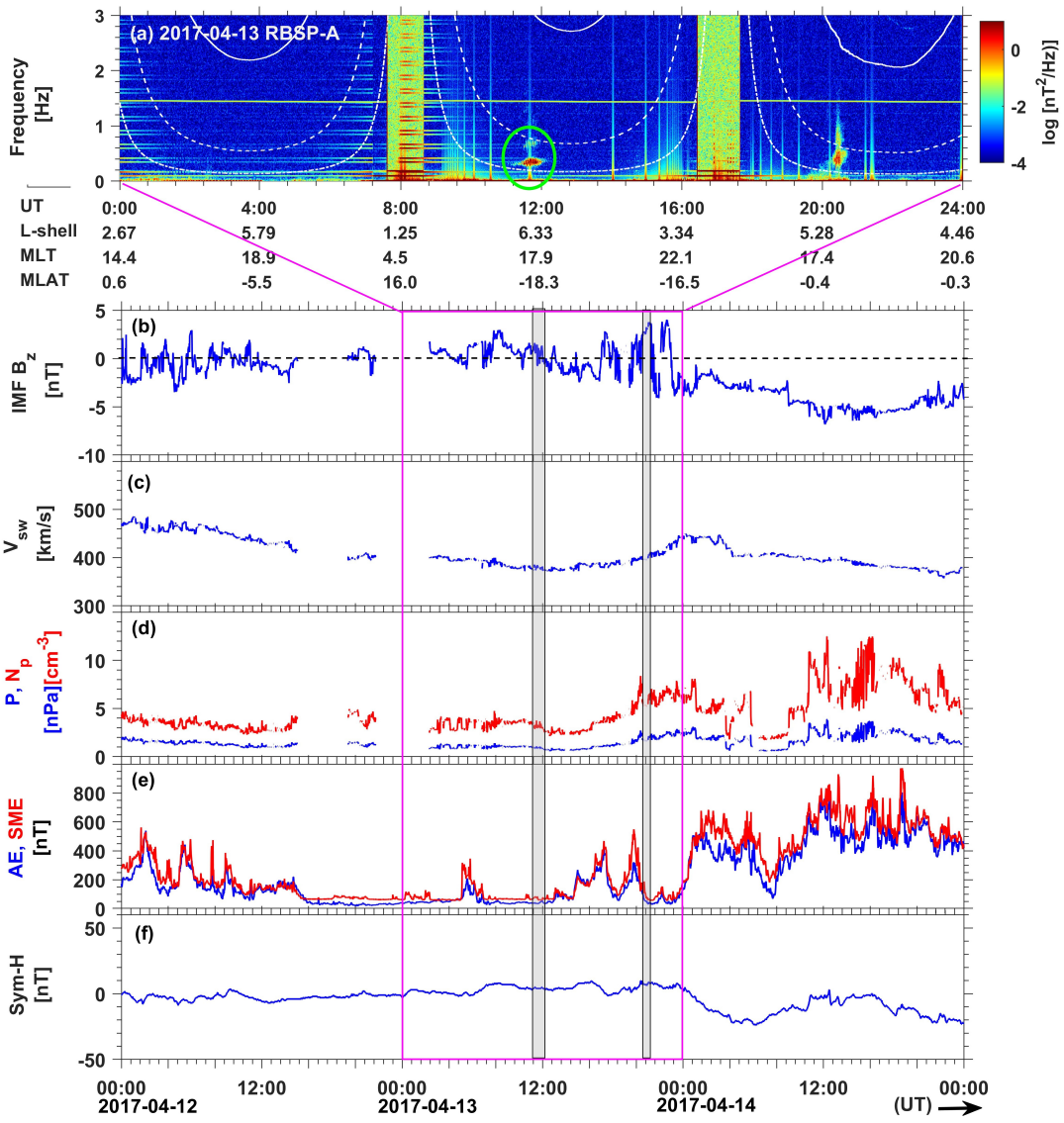

Figure 1: (a) Dynamic spectra showing EMIC waves observed by RBSP-A on 13 April 2017. A summary plot of interplanetary parameters and geomagnetic indices is shown for 12-14 April 2017 showing the intensely quiet period during the event in panels (b)-(f). The panels show (b) IMF B_z, (c) solar wind speed, (d) solar wind dynamic pressure P_{dyn} (blue) and solar wind proton density N_p (red) and (e) *AE* (blue) and *SME* (red) indices, and (f) *Sym-H* index. The pink rectangular box marks the event day, and the grey boxes show EMIC wave activities observed during the day. The wave event under discussion appears between 11:05-12:07 UT on 13 April 2017 and is marked in a green circle in the spectrogram. The x-axis of the spectrogram shows the position of RBSP-A with respect to time.

3.1 Event-01: 13 April 2017

3.1.1 EMIC Waves from Space

Figure 1(a) presents the spectrogram of the magnetic field data from RBSP-A during Event-01: 13 April 2017 showing EMIC waves. The white lines are the proton cyclotron frequency (solid), helium cyclotron frequency (dashed), and oxygen cyclotron frequency (dash-dotted line). The EMIC wave occurs during 11:05-12:07 UT on 13 April 2017 in the He^+ band between frequencies $\sim 0.27 - 0.47$ Hz. The spacecraft was located at L$\simeq$6.2, Magnetic Local Time (MLT) of $\sim$17.7 Hrs and $\sim -18^\circ$ magnetic latitude (MLAT) as indicated in the x-axis of the spectrogram. The wave attained a peak amplitude of 2.9 nT at around $\sim$11:52 UT. A higher frequency (harmonic-like feature) also appears in the He^+ band between $\sim 0.6 - 0.8$ Hz. RBSP-B followed RBSP-A $\sim$3 hrs later to sample similar L-shell and MLT locations, and slightly different MLAT ($\sim -12^\circ$), but did not observe any EMIC wave activity (not shown here).

3.1.2 Preconditioning the Magnetosphere

Solar wind parameters and geomagnetic indices corresponding to Event-01 are projected in Figure 1 (b) IMF B_z, (c) solar wind speed, (d) solar wind density (red) and dynamic pressure (blue) and geomagnetic indices (e) *AE* (blue) and *SME* (red) and (f) *Sym-H* for the duration of $\pm$1 day of the event, i.e., during 12-14 April 2017. The grey boxes indicate the EMIC wave activities observed during the day. The wave event under discussion is the first grey box, also marked by a green circle in panel (a) in the spectrogram.

For Event-01, the IMF B_z is slightly southward (minimum of -1.17 nT) for a very brief interval before the start of the event, turned northward just before the event, and stayed northward (1.5 nT) for most of the event duration. Solar wind flow speed slowly decreases from the start of 12 April, reaches a minimum of $\sim$ 380 km/s during the event, and increases thereafter. Solar wind density and dynamic pressure do not show any signature of a sudden increase (i.e., no signs of compression) and remain low ($<5\ cm^{-3}$ and $<$2 nPa, respectively) starting 12 April 2017 until the end of 13 April 2017.

The geomagnetic *AE* index drops to very quiet levels ($<$ 60 nT) around 16 UT on 12 April and stays quiet until the start of the event. A minor increase in the *AE* index is observed with a peak of *AE*$\simeq$203 nT at 05:35 UT where the SuperMAG auroral electrojet *SME* index, which uses a larger number of stations, shows a peak of *SME*$\simeq$346 nT. This increase could be associated with the auroral substorm onset at $\sim$05:03 UT identified by the SuperMAG list of substorms (Newell & Gjerloev, 2011a; Forsyth et al., 2015; Ohtani & Gjerloev, 2020). The *SME* index also shows a minor peak of $<$100 nT shortly before the wave activity. Geomagnetic *Sym-H* index stays relatively constant and close to zero ($|$*Sym-H*$| <$ 10 nT) during 12-13 April 2017. A small and gradual increase is, however, noticed during 6-8 UT in the *Sym-H* index from -2 to 8 nT, which indicates a possible slow compression on the dayside magnetosphere during this period. No corresponding enhancement is, however, observed in the solar wind dynamic pressure. Nevertheless, both the substorm signature and the slow, gradual compression occur multiple hours before the observed wave onset at the satellite.

3.1.3 EMIC Waves from Ground

While satellite observations tell us where the waves are seen in space, ground measurements, though dependent on the station location, can tell us the approximate length of time that the waves persisted. Figure 2 shows the spectrograms of magnetic field data from Induction (Search) Coil Magnetometer (ICM) at (a) Indian Antarctic station Maitri, and from Finnish Pulsation magnetometer network stations (b) Kilpisjärvi, (c) Ivalo, (d) Sodankylä and (e) Oulu for 13 April 2017. The grey shaded region shows the wave activity

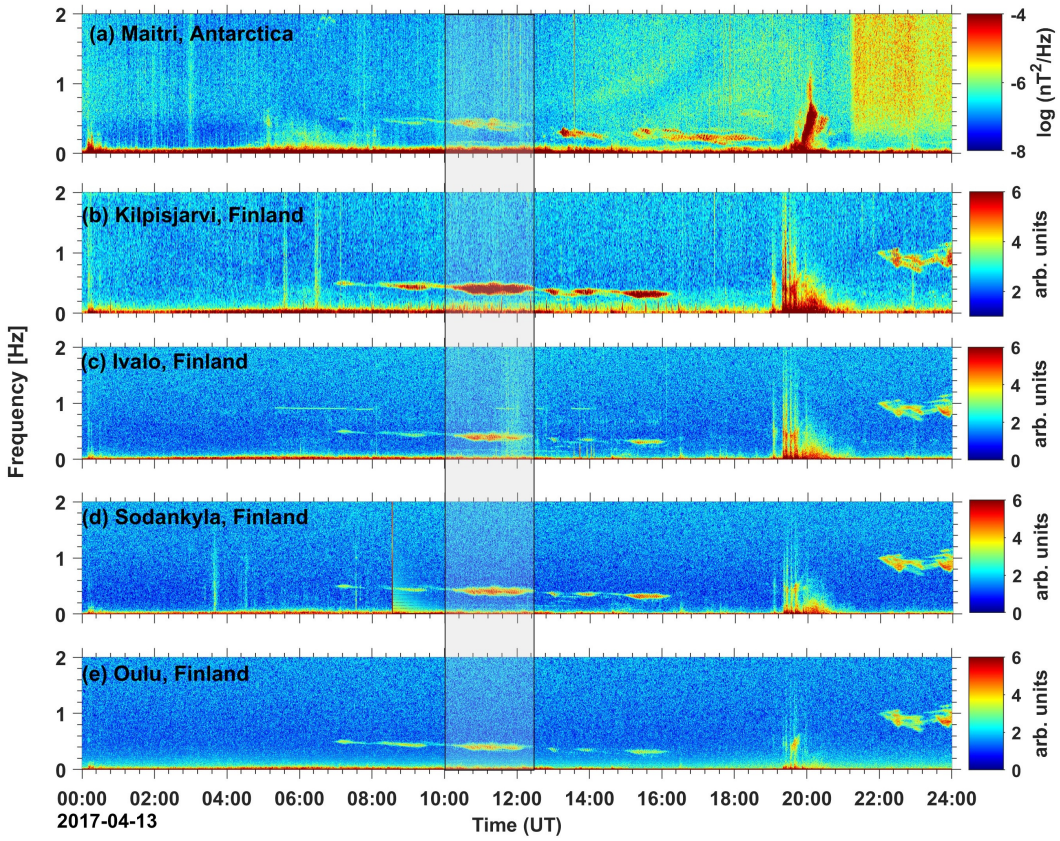

Figure 2: Dynamic spectra of ICM data from (a) Maitri, Antarctica, and from Finnish Pulsation magnetometer network stations (b) Kilpisjärvi (c) Ivalo (d) Sodankylä and (e) Oulu during 13 April 2017. The shaded area in the plot shows the EMIC event under discussion.

under discussion. The satellite footpoints and the ground station locations are given in Table S1 and Figure S1(a) in the Supporting Information.

The EMIC wave activity during the interval under discussion appears to have started at Maitri slightly after ∼10:00 UT, close to 0.5 Hz, and sustains until ∼12:24 UT when the station traverses the noon side MLT sector from ∼10:45-13:15 MLT. Weak wave patches are seen to appear earlier in the day, starting around ∼08:00 UT. The nearest available conjugate ground station to Maitri is Kilpisjärvi, Finland, which also sees wave activity during the same interval while the station was at ∼12 MLT (at 10:00 UT). Further stations in the similar longitude but lower L-shells are Ivalo, Sodankylä, and Oulu, wherein the wave activity appears during the same interval ∼10:00-12:24 UT. In all these stations, wave patches start to appear as early as ∼07:00 UT and sustain until ∼16 UT or later.

The footpoint of RBSP-A is east of the ground locations for this event. Hence, RBSP-A (and probably RBSP-B as well) was either potentially not in the right L and/or MLT sectors to observe these waves earlier, or these waves might be generated at different sources closer to noon MLT and propagated to ground locations at these longitudes. We cannot yet confidently identify whether these have the same wave source as the one observed by RBSP-A at dusk longitudes.

3.1.4 EMIC Wave Drivers

Figure 3 shows (a) magnetic spectra showing EMIC waves observed on RBSP-A for Event-01 (same as Figure 1(a)), (b) energy-time spectrogram of spin averaged proton flux and (c)-(i) pitch angle distributions (PADs) of ∼5.2 to 13.1-keV protons from HOPE. The interval of the EMIC wave activity is marked within the grey box. From panel (b) to (i), we can see a very small enhancement in the proton flux starting at ∼10:44 UT, just before the onset of the EMIC wave for energies ∼5.2 to 13.1 keV. The 90° peaked PA distributions are visible for the 5-11 keV energies with an energy-dependent time delay. The 13.1 keV energy channel shows a butterfly distribution pre-event and a field-aligned distribution during the event. As can be seen, the increase in flux is very small and limited to lower energy channels. The PADs of higher energy channels from HOPE are plotted in Figure S2 in the Supporting Information (SI). The flux increases are not significant in higher energy channels, either from HOPE or MagEIS (not shown). The onset of the wave at ∼11:05 UT does not precisely match the enhancement of these particle fluxes starting at ∼10:44 UT.

The LANL geostationary spacecraft are further checked for injection signatures or low-energy proton flux enhancements, or dipolarizations. Before and during the EMIC wave period, there is no indication of an ion injection or ion flux enhancements by any duskside LANL spacecraft (see Figure S3 in SI). Other geostationary satellites, GOES-13 and -15, were in the dawn sector during the event period and did not see any EMIC wave activity, flux enhancement, or signature of dipolarization associated with this event (not shown).

The four Cluster spacecraft (Escoubet et al., 2001) entered the magnetosphere from the magnetosheath between 10:00 and 13:00 UT on 13 April 2017. As the spacecraft were on the morning side of the magnetosphere (8 MLT), data were analyzed to see if there were signatures of the dayside compression. The four spacecraft observed a similar event: a smooth magnetosphere entry between 10:32 and 10:33 UT and a more abrupt jump into the magnetosheath at 10:37 (see Text S4 and Figure S4 in SI for more details on Cluster observations). The smooth transition is seen with the progressive disappearance of magnetosheath particles. A sharp change in the particle energy and the magnetic field magnitude marks the return in the magnetosheath. This quick change seen in the four spacecraft is typical of magnetospheric compressions. This compression event is short as C4 is again entering the magnetosphere two minutes later. Thus, one can conclude that a local magnetosphere compression event at 10:36 UT, possibly linked with a local pressure pulse, shortly takes the four Cluster spacecraft out of the magnetosphere. This small pressure pulse, which was not seen in OMNI data nor in *Sym-H* data, is not sufficient to explain the intense, long-lasting

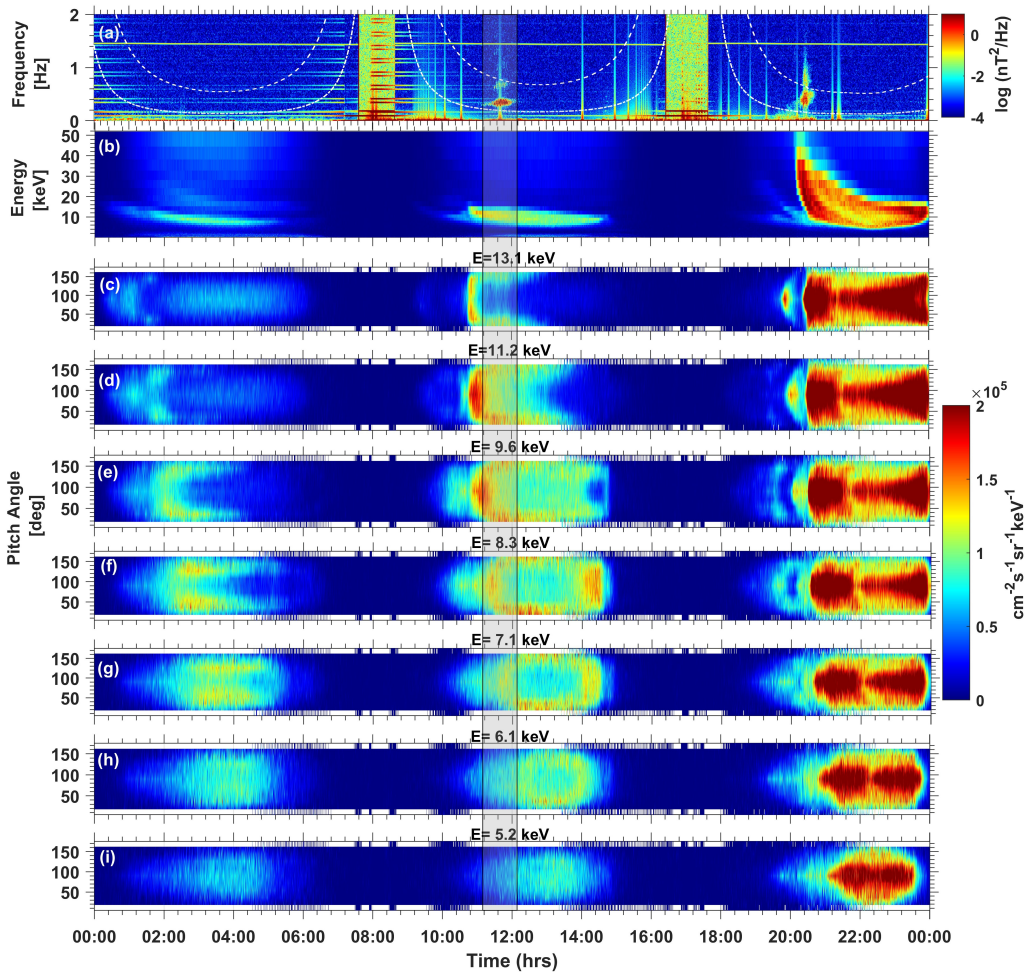

Figure 3: (a) Dynamic spectra showing EMIC waves on 13 April 2017 (same as in Figure 1(a)). (b) Energy-Time spectrogram of spin-averaged protons as observed by HOPE on board RBSP-A. The pitch angle distributions (PADs) of ∼5.2 to 13.1-keV protons as observed by HOPE on board RBSP-A are shown in panels (c) to (i).

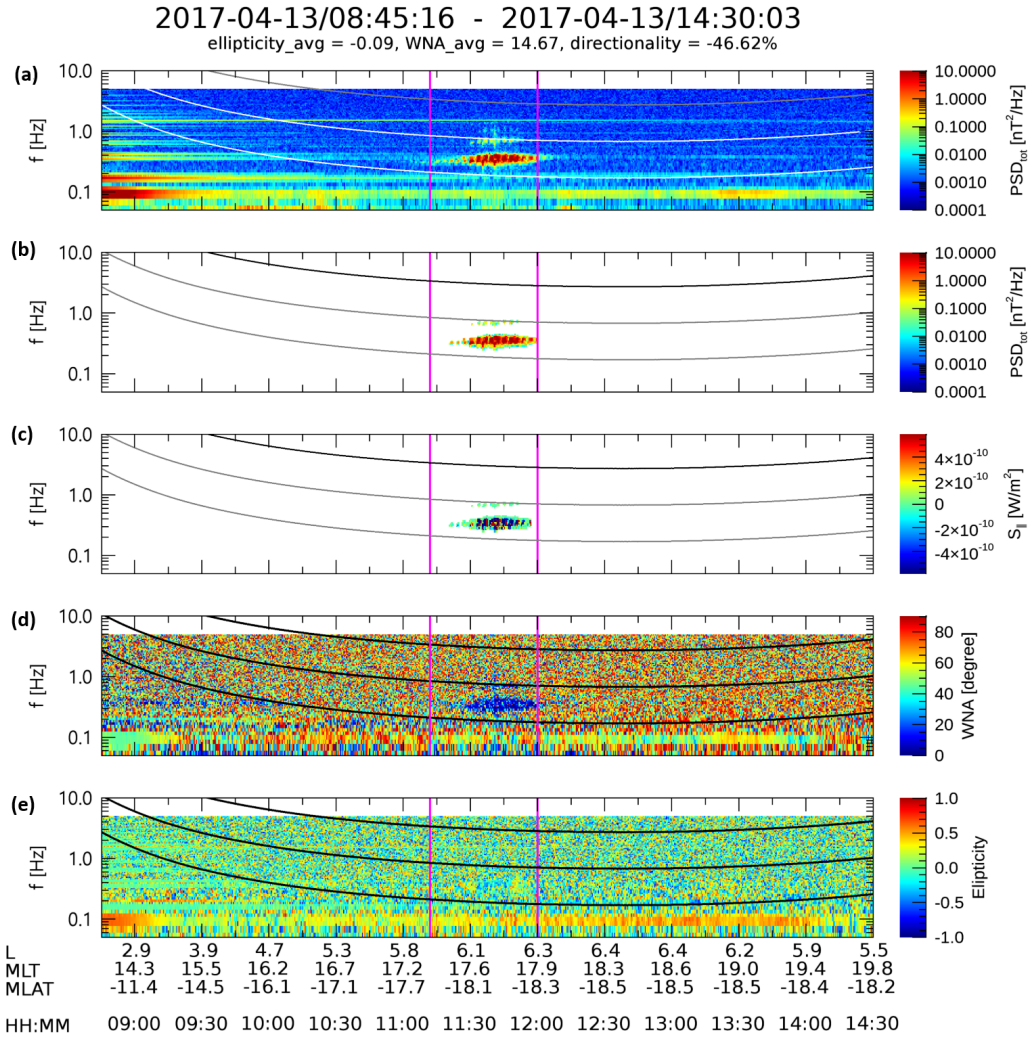

Figure 4: Poynting flux and polarization analysis of Event-01 on 13 April 2017. (a-b) Dynamic spectra of magnetic field showing EMIC waves (c) Poynting flux calculations showing direction of the energy propagation with respect to the background magnetic field direction (d) Wave normal angle (WNA) and (e) Ellipticity ϵ of the EMIC waves during the interval 08:45 to 14:30 on 13 April 2017.

EMIC waves observed in the evening MLT sector but may be a partial explanation for the waves observed at earlier hours from the ground stations.

3.1.5 Wave Generation and Free Energy

For the EMIC wave event observed on 13 April 2017 between 11:05-12:07 UT, the *AE* index shows a minor peak of $\sim$ 203 nT (*SME*$\simeq$346 nT) at the start of the day around $\sim$05:35 UT which is associated with the substorm onset at $\sim$05:03 UT identified by SuperMAG list of substorms. The *AE* index was $<$ 50 nT (*SME*$<$100 nT), well below the quiet geomagnetic levels later and throughout the event. It is important to note that while the substorm onset is recorded at $\sim$05:03 UT, the earliest observations of wave activity at ground locations is at $\sim$07 UT, and the wave is first observed in space between 11:05-12:07 UT. RBSP-A

was unlikely to be in the right place to observe the wave at the beginning of the event, and the ground stations may also not have been in the correct sector either. However, the multiple-hour delay between the substorm onset and observations of the waves is perplexing.

A minor flux enhancement for 6-13 keV energy protons is visible in the HOPE PA resolved plots (Figure 3) during the EMIC wave activity. However, the enhancement does not have a one-to-one association with the wave onset. Also, no signature of an injection/flux enhancement is observed by the geostationary satellites. Since the space environment was so inactive, this little increase in the auroral indices earlier on the day and the quick, small change in the IMF B_z closer to the start of the event were possibly sufficient enough to provide a substorm/injection-like response at some energies.

In order to confidently identify the wave drivers, it is important to know whether the waves are locally generated or propagated from elsewhere. The wave during Event-01 (13 April 2017) is observed at $\sim -18^\circ$ MLAT, and hence it is likely that the waves were generated near equatorial latitudes and propagated along the field lines to be observed at the off-equatorial satellite location. A polarization analysis is done to identify the wave source region, which is displayed in Figure 4. Panels show (a and b) EMIC wave dynamic spectrogram showing the power spectral density, (c) Poynting flux calculated along the field line, (d) wave normal angle (WNA), and (e) ellipticity ϵ during the wave interval. The sign of the Poynting flux is the direction of the energy propagation with respect to the background magnetic field direction. The directionality mentioned at the top of the figure shows the percentage of the wave energy propagation for a given wave packet, which is -47% for this event. It is calculated as the ratio of the sum of the time and frequency averaged Poynting flux in the wave interval to that of the absolute Poynting flux. The Poynting vectors from panel (c) are close to zero (green) at the start of the wave onset and a mixture of positive and negative (red and blue) values during the rest of the wave activity. This indicates that the wave energy flow is bi-directional, or in other words, the wave is at the generation region. The low wave normal angle (average WNA$\sim 14^\circ$) showing field-aligned propagation also supports that the wave is close to the source region or is locally generated. However, very low ellipticity values (average $\sim \epsilon = -0.09$) indicate linear polarization of the waves, which is not expected for waves observed at the source region.

We now test the possibility of the scenario in which the waves were locally generated. Figure 5 shows proton drift trajectories for two different values of μ (first adiabatic invariant) corresponding to (a) 10 keV and (b) 15 keV. The K value is chosen to be $0.0024\mathrm{G}^{0.5}R_E$, which corresponds to an equatorial pitch-angle of 85° at L=5.5. These drifts are obtained assuming the Weimer electric field model (Weimer, 2005) and the Tsyganenko 1989 magnetic field model (Tsyganenko, 1989). The color bar shows drift time in hours. The starting point of the trajectory, 05:03 UT, MLT=23, and L=5.5, is marked as a cross, and the RBSP-A location (MLT=17.5, L=6) during Event-01 (13 April 2017) is indicated by a circle. It can be seen that the 10-15 keV protons need several hours (∼3-5 hrs) to drift from the night side to the dusk sector where EMIC waves are observed. This indicates a possibility that protons injected during the substorm at ∼05:03 UT drifted duskward and generated EMIC waves hours later. It also suggests that using a 30-60 minute duration from substorm onset as the impact time of substorm dynamics on the inner magnetosphere may need to be adjusted. During periods of very quiet solar wind, the lower energy protons of a substorm injection drift slowly in MLT, and thus it may be hours after substorm onset before these protons provide the required ion composition, ion flux, and ion temperature anisotropy to generate EMIC waves. When the magnetosphere is more active, perhaps other dynamics disrupt the injection, and its not as large/prevalent when it finally reaches the inner magnetosphere. However, during very quiet periods, injected protons can make it hours later to the regions where they can then generate the EMIC wave at amplitudes observable to the instrumentation/identification thresholds.

Assuming that we have identified the probable driver for this event (the injection), we now look at whether there was sufficient temperature anisotropy to feed the wave growth.

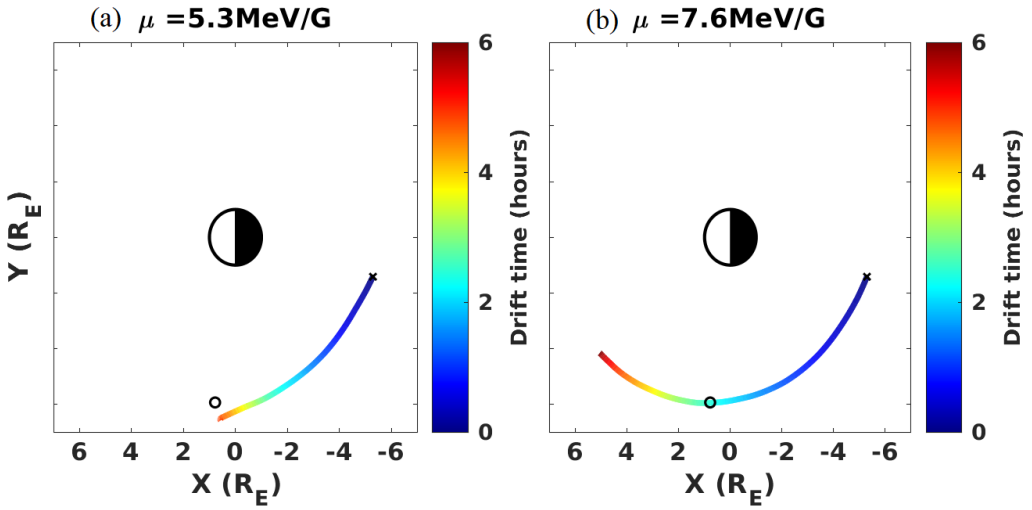

Figure 5: Proton drift trajectories corresponding to Event-01 on 13 April 2017 for μ values corresponding to (a) 10 keV and (b) 15 keV, respectively, at L=5.5 and K=0.0024G$^{0.5}R_E$. Color-bar shows the drift time in hours. The cross is the starting point of the trajectory, and the circle indicates approximate RBSP-A location (MLT=17.5, L=6).

The theory of resonant wave-particle interaction explains how waves resonate with particles at specific energies. While the normally used temperature moment anisotropy parameter (hereby denoted as A_{mom} and given by $A_{mom} = T_\perp/T_\parallel - 1$) represents the overall free energy condition in the particle distribution, it smooths out the anisotropic features that occur at specific energy ranges where resonance happens. The original anisotropy representation derived by Kennel and Petschek (1966) includes a resonant energy term. Thus, we can present the anisotropy parameter at specific parallel energies. We plot this Kennel-Petschek (KP) anisotropy parameter from 10 keV to 150 keV, covering the typical range of resonant energies for EMIC waves in the Earth's magnetosphere.

The KP anisotropy, critical for testing the Kennel-Petschek ion cyclotron instability criterion, is derived using proton observations obtained by RBSP-A following Noh et al. (2018). Proton flux measurements from HOPE (1 eV52 keV) and RBSPICE (52488 keV) are combined, followed by a coordinate transformation from the energy-pitch angle to gyrotropic velocity space. The KP anisotropy is then calculated by integrating the proton distributions, taking into account resonance conditions and an energy range up to 150 keV, which covers typical proton energies interacting with EMIC waves in the magnetosphere. To ensure the calculation accuracy, we require 60% data coverage in the perpendicular velocity direction. Further details of the KP anisotopy calculation can be found in Noh et al. (2018).

Figure 6(i) (panels a to c) shows the derived Kennel-Petschek anisotropy parameter (Kennel & Petschek, 1966) of the $10 - 150$ keV protons calculated using the HOPE and RBSPICE data for the wave event 13 April 2017 (Panels d-f will be discussed under the second event). Panel (a) shows the energy-time spectrogram of the derived KP anisotropy parameter (given by Equation 2 in (Noh et al., 2018)). Panels (b) and (c) show line plots of the KP anisotropy parameter for different energy channels. Different colours indicate different proton parallel energies as indicated on the right side of the panels. A_{mom} obtained from the moment calculations of the HOPE and RBSPICE observations is also plotted as the grey line in panels (b and c) for comparison. The green lines represent the parallel proton beta $\beta_{\parallel,p}$, which is indicated by the right-hand side y-axis. Note that the different

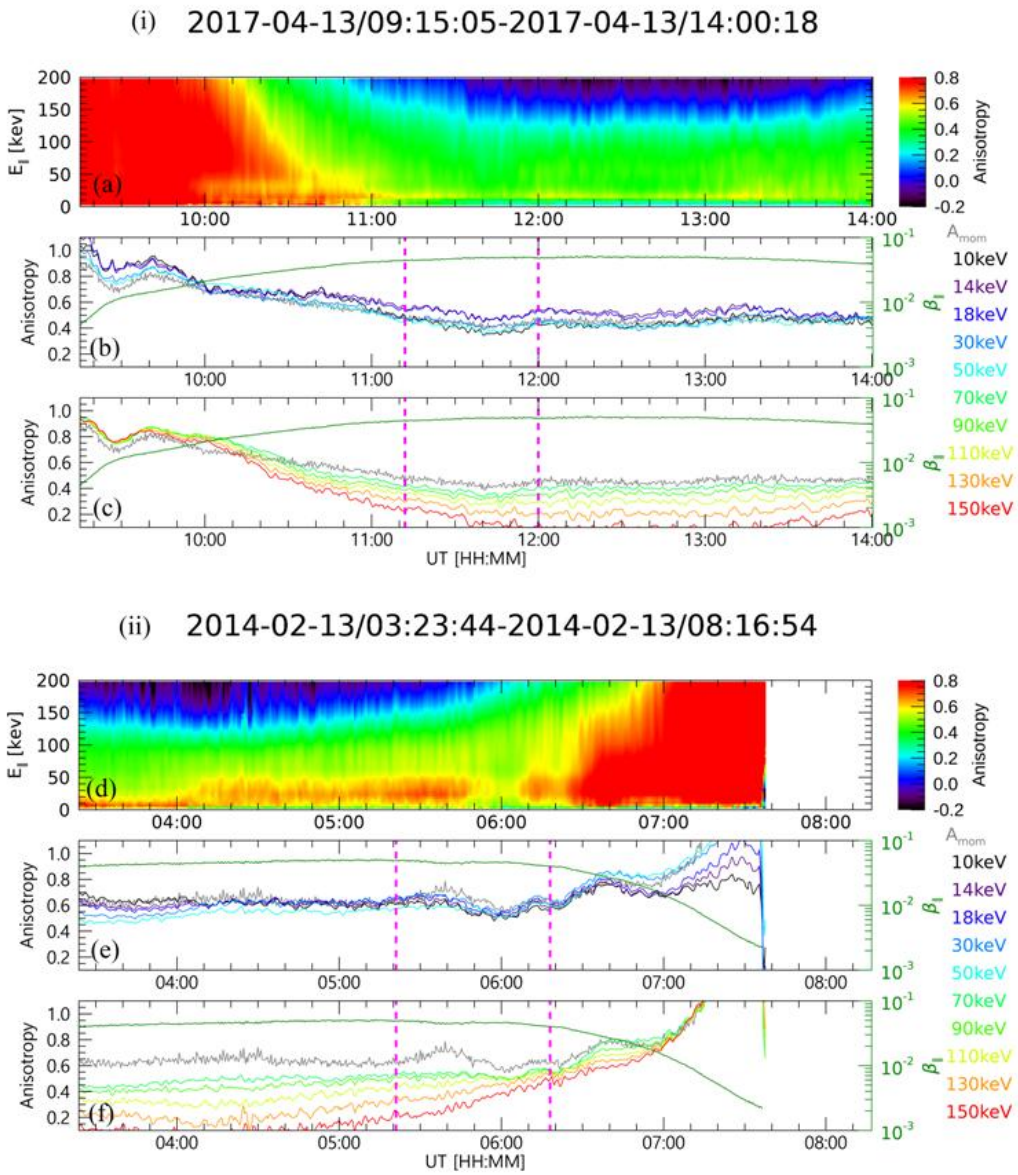

Figure 6: (a) Energy-time spectrogram showing the derived Kennel-Petschek (KP) anisotropy parameter of protons from HOPE and RBSPICE instruments is shown for the event on (i) 13 April 2017. The calculated KP anisotropy parameter for different energy channels is shown in panels (b) and (c), where the energies are distinguished by colour. The grey lines in these panels refer to the temperature moment anisotropy (A_{mom}) obtained by combining the HOPE and RBSPICE moment calculations during this event. The green lines represent the parallel proton beta $\beta_{\parallel,p}$ indicated by the right-hand y-axis in these panels. The panels (d-f) represent the same as panels (a-c), respectively, for the event on (ii) 13 February 2014.

energy channels are divided across the two bottom panels for visual clarity. In each of the two bottom panels (b and c), the A_{mom} (grey) and parallel proton beta (green) lines are repeated for reference. The pink vertical lines mark the start and end time of the event. From the panels, both the moment anisotropy and the KP anisotropy show no significant changes around or at the start of the wave event. This suggests that the particle distribution does not show any evident additional free energy for the wave growth. A relatively smooth variation of the KP anisotropy is observed across almost all energies, with its good agreement with the moment anisotropy A_{mom} indicating that there is no clear change in the particle distribution.

So, what is the free energy for driving these waves? In their paper, Noh et al. (2018) calculated the proton anisotropy parameter for EMIC events using RBSP-A observations. They found that the anisotropy values are often slightly larger immediately after EMIC wave onsets. However, this increase in anisotropy is rather very small, but discernible. Their study also suggests that proton distributions often remain near a marginal state, with anisotropies close to threshold values for ion cyclotron instability. The anisotropy values observed in this study are also positive and hence could be in a marginal condition to feed the necessary free energy for ion cyclotron instability.

The waves started to appear on ground stations earlier that day. A possible driver candidate for these earlier waves could be the slow, gradual compression of the dayside magnetosphere indicated by an increase of ∼10 nT in the *Sym-H* index during 6-8 UT and a local magnetosphere compression event at 10:36 UT observed by Cluster. The wave onsets at the ground stations are time-correlated with this possible compression of the magnetosphere. Additionally, perhaps the small compression also helped enhance the temperature anisotropy of substorm-injected protons as they drifted around the magnetosphere. Thus, perhaps the combined effect of the long-duration injection with the pressure pulse was sufficient to generate the large-amplitude EMIC wave observed in situ.

3.2 Event-02: 13 February 2014

3.2.1 EMIC Waves from Space

Figure 7 shows EMIC wave activity and corresponding solar wind and geomagnetic parameters during Event-02 on 13 February 2014. The panels are the same as in Figure 1. From Figure 7(a), the wave appears during 05:19-06:18 UT (marked as green circle in the spectrogram) in the He^+ band between $\sim 0.2-0.55$ Hz and attains a peak amplitude of 2.33 nT at around ∼05:30 UT. The spacecraft was located post-noon at ∼13.3 MLT with L≃6.0 and $\sim -17.3°$ MLAT as can be seen from the location of RBSP-A indicated in the x-axis of the spectrogram. RBSP-B preceded RBSP-A by ∼3 hrs and sampled similar L-shell and MLT locations (MLAT $\sim -14°$), nevertheless, it did not observe any EMIC wave activity in that orbit (not shown here).

EMIC waves are observed again in the following orbit in the dayside MLT sector, which is associated with a sudden impulse in the magnetospheric pressure and density as identified from the solar wind parameters.

3.2.2 Preconditioning the Magnetosphere

IMF B_z turned northward at $\sim$ 17 UT on the day prior to the event (12 February) and stayed northward ($>$ 5 nT) for all of 13 February 2014, before turning southward post 14:00 UT on 14 February 2014. The flow speed is slowly reducing during 12-13 February, while density and dynamic pressure remain very low (<4 cm^{-3} and $<$ 1 nPa, respectively) starting at noon on the previous day until much later after the event. However, there is a minor increase in density from 1.3 to 3.9 cm^{-3} (0.47 to 1.1 nPa in dynamic pressure), during the beginning of the day from ∼00:10 to 04:00 UT and remains at these values throughout the event. These increased pressure and density values are still much below the threshold

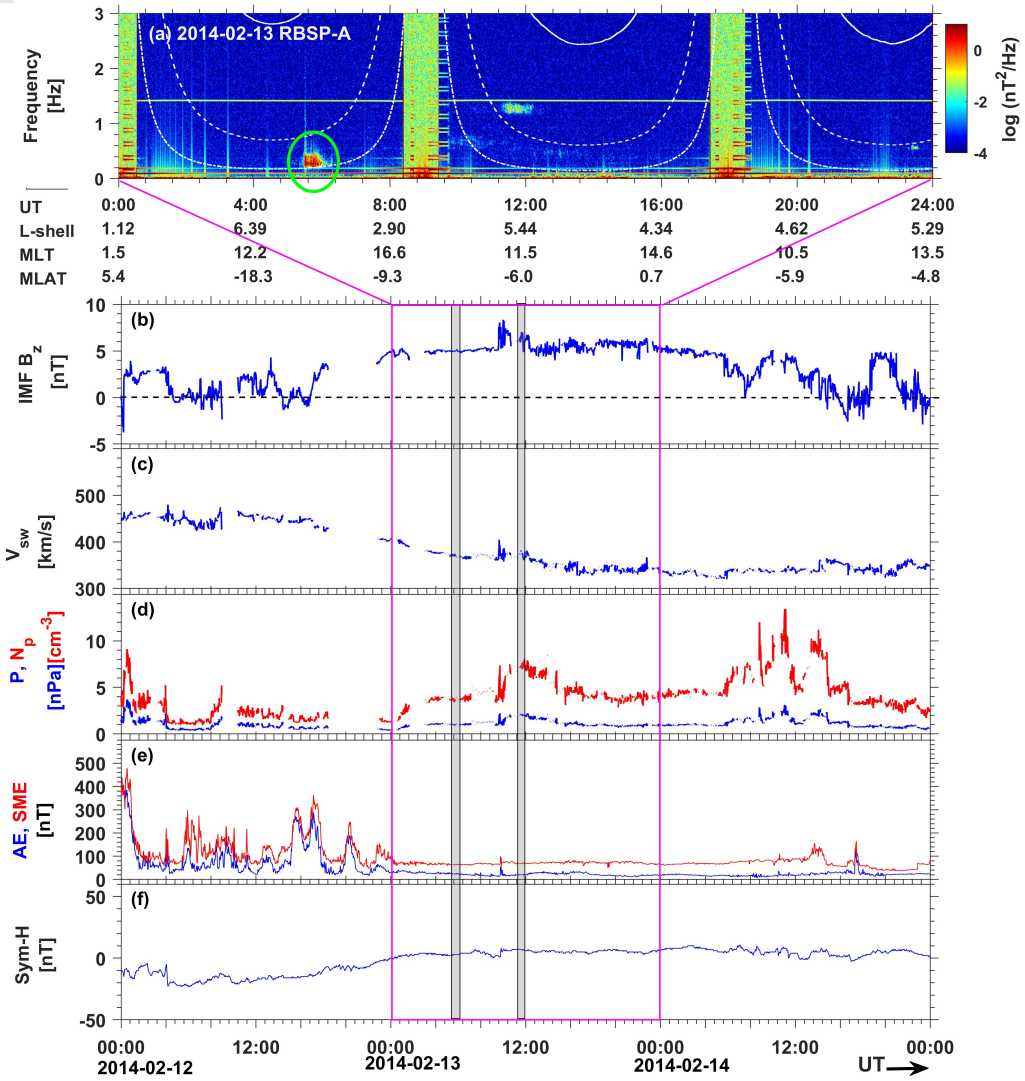

Figure 7: (a) Dynamic spectra showing EMIC waves observed by RBSP-A on 13 February 2014. A summary plot of interplanetary parameters and geomagnetic indices is shown for 12-14 February 2014, showing the intensely quiet period during the event. The panels show (b) IMF B_z, (c) solar wind speed, (d) solar wind dynamic pressure P_{dyn} (blue) and solar wind proton density N_p (red) and geomagnetic indices (e) *AE* (blue) and *SME* (red) indices, and (f) *Sym-H*. The pink rectangular box marks the event day, and the grey boxes show EMIC wave activities observed during the day. The wave event under discussion appears between 05:19-06:18 UT on 13 February 2014 and is marked in a green circle in the spectrogram. The x-axis of the spectrogram shows the position of RBSP-A with respect to time.

values usually considered for active/unstable magnetosphere (e.g., Usanova et al., 2012; Min et al., 2012, and references therein). *AE* remains at very quiet levels (< 50 nT) starting ∼23 UT on 12 February until the end of 14 February. The *SME* index also lies below 100 nT starting 23 UT on 12 February until 12 UT of 14 February. The *Sym-H* index stays relatively constant $|Sym\text{-}H| < 10$ nT during 12-15 February 2014.

3.2.3 EMIC Waves from Ground

Figure 8 shows the spectrograms of magnetic field data from the ICM array of CARISMA network stations Dawson city (DAWS), Fort Churchill (FCHU), Ministik Lake (MSTK), Pinawa (PINA), and Rabbit Lake (RABB) (a-e), and ISEE magnetometer network stations (Shiokawa et al., 2010) Athabasca (ATH), Magadan (MGD), Moshiri (MSR) and Paratunka (PTK) (f-i), during Event-02 on 13 February 2014. The satellite footpoints and the ground locations are given in Table S2 and Figure S1 (b) in the Supporting Information.

The Pc1 wave event starts around ∼01:15 UT at stations DAWS, MSTK, RABB, and ATH (∼18 MLT) and FCHU (∼19 MLT) and sustains until ∼04:00 UT. The wave starts to appear at stations PINA (and ISLL and THRF in similar longitudes-not shown here) slightly later, around ∼02:00 UT (∼20 MLT local time). Station FCHU, though, is in a similar longitude as ISLL, PINA, and THRF, but at a higher geomagnetic latitude of 68.3°N, sees the wave around ∼01:15 UT. It is possible that the waves were ducted to lower latitudes and hence appear late in lower latitude stations. The stations at MSR, MGD, and PTK started to see the wave around ∼03:30 UT when the stations moved to the noon-dusk local time sector (∼12:30, 14:30, and 15:30 MLT, respectively). RBSP-A was westward of the ground stations and observed the wave activity at a later time interval (∼05:19 UT) as it traversed the noon MLT sector.

3.2.4 EMIC Wave Drivers

Figure 9 shows measurements during 13 February 2014 in the same format as in Figure 3. Panels show (a) EMIC wave observed on RBSP-A for 13 February 2014, (b) shows energy-time spectrogram of spin-averaged proton flux from HOPE, and PADs of 5 to 52-keV protons in panels (c)-(h). The interval of the EMIC wave activity is marked within the grey box. From panels (b) to (h), it can be noted that no significant signatures of particle injections are visible at the onset or before the wave onset. There is a very weak signature of flux enhancement towards the end of the orbit for energies between 15-22 keV, however, it is considerably lower as compared to the previous event and does not have a one-to-one correlation with the wave onset time.

3.2.5 Wave Generation and Free Energy

For Event-02 on 13 February 2014 from 05:19-06:18 UT, there is no indication of any substorm or injection-like signature associated with the wave onset from geostationary satellites, RBSP-A or RBSP-B, or from geomagnetic indices and solar wind parameters. The density and dynamic pressure values remain constant (∼4 cm^{-3} and ∼1 nPa, respectively) before, during, and much later after the event. However, a closer analysis of these plots shows a gradual increase in density from 1.3 to 3.9 cm^{-3} and dynamic pressure from 0.47 to 1.1 nPa during the beginning of the day, peaking at ∼04:00 UT. This observed increase was slow and gradual over ∼3.5 hours, and the values are still much below the otherwise active threshold values ($P_{dyn} < 3$ nPa). However, these enhanced values are more than double their initial values and could possibly indicate a slow, gradual, but small compression of the magnetosphere. Since the space environment was so quiet, this small and gradual increase in the dynamic pressure was possibly sufficient enough to trigger the EMIC instability condition.

The Pc1 signatures at the ground stations indicate that the waves started to appear earliest at ∼01:00 UT, which matches well with the timing of the gradual compression of the

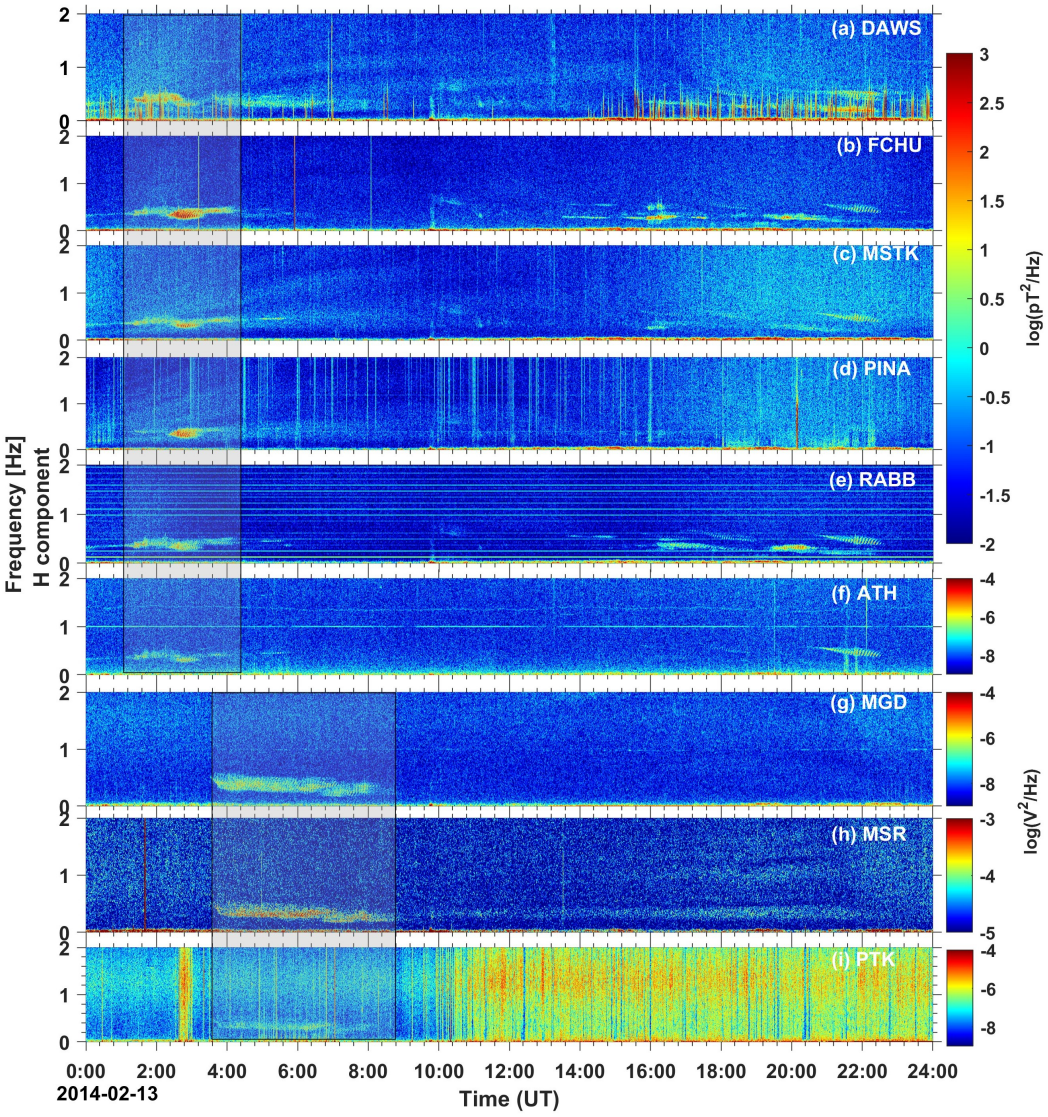

Figure 8: Fourier spectrograms of ICM data from CARISMA networks stations (a) DAWS, (b) FCHU, (c) MSTK, (d) PINA, and (e) RABB and ISEE ground magnetometer network stations (f) ATH, (g) MGD, (h) MSR, and (i) PTK, during 13 February 2014. The shaded area in the plot shows the EMIC event under discussion.

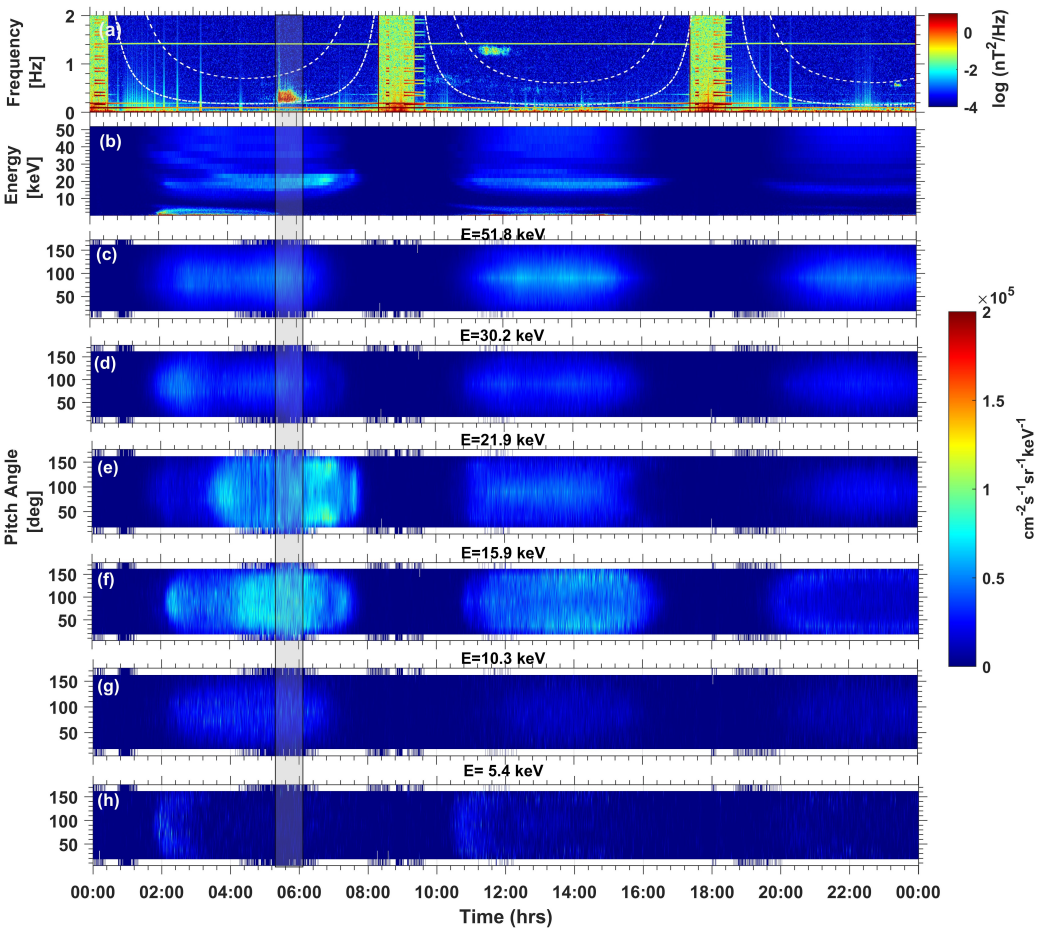

Figure 9: (a) Dynamic spectra showing EMIC waves on 13 February 2014 (same as in Figure 7(a)). (b) Energy-Time spectrogram of spin-averaged protons as observed by HOPE on board RBSP-A. The pitch angle distributions (PADs) of 5 to 52-keV protons as observed by HOPE on board RBSP-A are shown in panels (c) to (h).

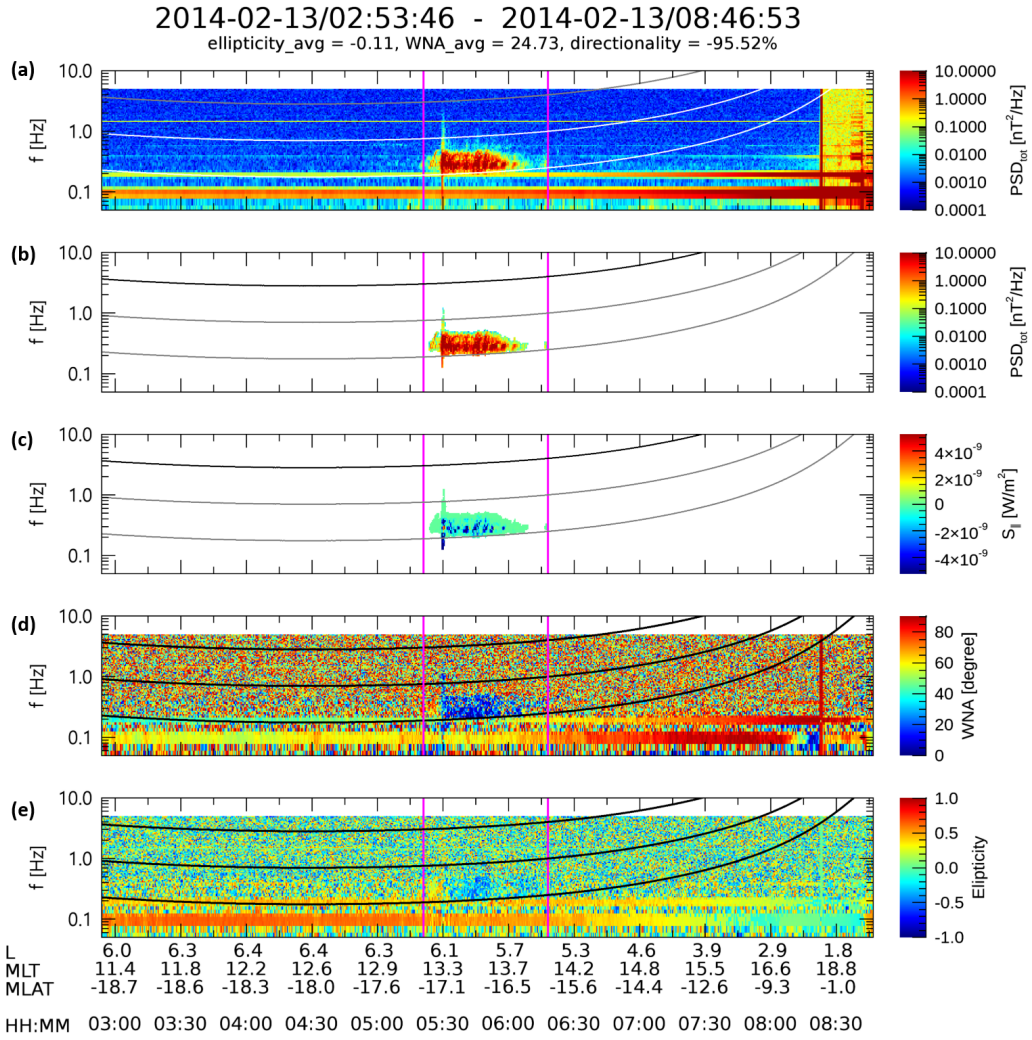

Figure 10: Poynting flux and polarization analysis of Event-02 on 13 February 2014. (a-b) Dynamic spectra of magnetic field showing EMIC waves (c) Poynting flux calculations showing direction of the energy propagation with respect to the background magnetic field direction (d) Wave normal angle (WNA) and (e) Ellipticity ϵ of the EMIC waves during the interval 03:00 to 08:30 on 13 February 2014.

magnetosphere. This would indicate that the wave was generated earlier that day, around ∼01:00 UT as the magnetosphere was compressed, and sustained for several hours in the magnetosphere, to be observed by RBSP-A hours later when it sampled the dayside wave generation region. However, RBSP-B does not observe the wave activity when it samples the same L and MLT locations in its previous orbit.

The wave during 13 February 2014 is observed at $\sim -17°$ MLAT, and hence it is likely that the waves generated near equatorial latitudes are propagated along the field lines to be observed at the off-equatorial satellite location. The polarization analysis for this event is displayed in Figure 10. Panels show (a and b) EMIC wave dynamic spectrogram showing the power spectral density, (c) Poynting flux calculated along the field line, (d) WNA, and (e) ellipticity ϵ during the wave interval. The Poynting vectors in panel (c) show a

mixture of zero (green) and negative (blue) values during the wave activity. The zero values indicate a bi-directional energy flow, and negative values indicate that the wave energy flow is southward. The majority of Poynting flux values are close to zero, indicating the wave is closer to the source region. A low wave normal angle (average WNA$\sim 24^{\circ}$) in panel (d), showing field-aligned propagation, supports the idea that the wave is close to the source region. The event is hence observed slightly away (to the south) but still close to the actual generation region. The ellipticity shows a mixture of left-hand and linear polarization.

Assuming that this event is driven by an extremely weak compression of the dayside magnetosphere, we now check whether there was sufficient temperature anisotropy to feed the wave growth. Figure 6(d-f) shows the derived Kennel-Petschek (KP) anisotropy parameter of $10-150$ keV protons for the wave event on 13 February 2014. The panels are in the same order and represent the same parameters as described for Event-01. There is a small increase in the KP anisotropy parameter evident at lower energy channels for <30 keV and a clear increase in the temperature moment anisotropy A_{mom} (grey line) during or at the onset of EMIC wave activity. This local increase in anisotropy supports the idea that the waves are near the source region. However, no driver has been identified for this observed additional free energy. The positive anisotropy values indicate that the magnetosphere was indeed under marginal EMIC wave instability conditions. The event also corroborates the idea that the dayside magnetosphere is indeed often marginally unstable to EMIC waves and can be driven unstable even by modest compressions (Anderson & Hamilton, 1993; Engebretson et al., 2002).

4 Summary and Conclusions

The free energy source for EMIC waves is commonly understood to be the anisotropic $1-100$ keV protons, which become unstable either during dayside magnetospheric compression, owing primarily to solar wind pressure pulses, or during nightside injections owing to geomagnetic storms/substorms. However, a subset of large amplitude EMIC events are found to be isolated and not associated with any clear evidence of these known drivers. These unique events thus drive questions about how such large amplitude EMIC waves can be generated within such a quiet magnetosphere and how often this may happen.

In this study, we demonstrate the magnetospheric conditions and provide possible drivers for two such quiet time, large amplitude EMIC wave events on 13 April 2017 and 13 February 2014 from available multi-point datasets. None of the aforementioned drivers of EMIC waves are evident for these events: no simultaneous substorm activity, within a few hours of the wave onset, no geomagnetic storm, and no clear pressure pulse confidently identified within the solar wind. However, a combination of a substorm occurring multiple hours ($\sim$6 hrs) prior to the event, extremely weak and gradual pressure increase at the solar wind, and the pre-conditioning of the inner magnetosphere can all provide additive effects, potentially resulting in the generation of such large-amplitude EMIC waves under quiet magnetospheric conditions. These identified drivers are not novel and fall under the traditionally known quiet time EMIC wave drivers, a weak substorm hours before the wave onset, or a small gradual pressure enhancement. However, it is noteworthy that such weak and otherwise insignificant pressure values and/or substorm injections occurring can play a significant role in wave generation during quiet conditions. We believe that there is a need to re-evaluate the impact time of substorm dynamics on the inner magnetosphere and what is considered an empirically sufficient wave driving pressure enhancement, especially for the quiet magnetospheric conditions. There is still a need to investigate further the possible drivers for such large amplitude quiet-time events, and we need more studies for a better understanding of quiet-time magnetospheric dynamics.

To summarize: The solar wind and geomagnetic parameters during the start of both the events under consideration indicate extremely quiet solar wind and magnetosphere; northward IMF B_z (<5 nT), gradually decreasing solar wind speed ($<$ 380 km/s), very low

solar wind density and dynamic pressure (<5 cm^{-3} and <2 nPa, respectively), geomagnetically quiet *AE* (< 60 nT) (or *SME* <100 nT) levels and relatively constant and close to zero *Sym-H* values (|*Sym-H*| < 10 nT), with no clear signatures of any known EMIC wave drivers. Thus, the question becomes, what was the free energy source for the observed high-amplitude EMIC wave growth? Was the magnetosphere and solar wind so quiet that only a small change was needed to generate the EMIC wave? Is the magnetosphere often so close to the instability threshold that any little push can generate such large amplitude waves?

1. **Possible driver/s for the 13 April 2017 EMIC event**:
   - The exiguous flux enhancement for 6-13 keV energy protons, a weak substorm activity multiple hours (∼6 hrs) before the wave onset and a quick small change in the IMF B_z just before the event, was probably sufficient to provide a substorm/injection-like response for this dusk sector EMIC wave excitation.
2. **Possible driver/s for the 13 February 2014 EMIC event**:
   - A nominal, slow and gradual increase in the dynamic pressure, which otherwise is negligible and much below the active threshold values (P_{dyn} << 3 nPa), could have possibly provided sufficient free energy to excite this noon sector EMIC wave. The waves must have sustained in the magnetosphere in order to have been observed hours later by RBSP-A as it traversed the noon local time sector.

It is possible that, with the scarcity of data coverage, both on the ground and in space, we might not be able to capture these drivers for all such events if the magnetosphere is indeed always close to the instability threshold. This study emphasizes the importance of studying the quiet time magnetosphere to understand different EMIC-related regimes under such quiet conditions: why some weak magnetic substorms or small, gradual pressure enhancements can produce intense, long-lasting EMIC wave events when a large majority don't. With the available datasets, it is not always possible to confidently identify whether the waves were locally generated or propagated. Ray tracing techniques can be used to identify the wave generation region, which is, however, beyond the scope of this paper. It is noteworthy that such weak substorm driven EMIC waves may take a long time to show up after their initial driver (i.e., substorm injection) as they are dependent on the injections of the warm/hot protons, which take longer to arrive than the electrons for chorus waves.

This work also asserts the significance of satellite-ground conjugate studies so that we not only understand where the waves are seen in space but also approximately when the wave was excited. It also highlights the need for more magnetospheric space missions and wider ground magnetometer coverage to understand the full extent of the wave behavior.

5 Open Research

The Van Allen Probes data are available at `https://emfisis.physics.uiowa.edu/data/index` for EMFISIS and `https://rbsp-ect.newmexicoconsortium.org/science/DataDirectories.php` for HOPE, MagEIS, and REPT. Geomagnetic activity data are obtained from `http://wdc.kugi.kyoto-u.ac.jp/kp/index.html` and OMNI solar wind parameters from `https://spdf.gsfc.nasa.gov/pub/data/omni/`. CARISMA ICM data can be accessed at `https://data.carisma.ca/`. The ICM data from ISEE magnetometer network are available at `https://ergsc.isee.nagoya-u.ac.jp/data/ergsc/ground/geomag/isee/`. The authors thank Tero Raita for SGO data access and the overview plots can be found at `https://www.sgo.fi/Data/Pulsation/pulArchive.php`. The SuperMAG substorm lists are available at `https://supermag.jhuapl.edu/substorms/`. The Cluster plots have been adapted from the Cluster Science Archive `https://www.cosmos.esa.int/web/csa/`. The Maitri magnetometer data can be accessed at Zenodo via `https://doi.org/10.5281/zenodo.13149317` (Remya, 2024b). The LANL data used in this work can be ac-

cessed at Zenodo via https://zenodo.org/records/12629463 (Henderson, 2024). The EMIC event list used in this study can be accessed at Zenodo via https://doi.org/10.5281/zenodo.14195258 (Remya, 2024a). The L-shell and geomagnetic coordinates corresponding to the ground stations are calculated for each event period using https://www.geomagsphere.org/index.php/l-shell-calculator and https://wdc.kugi.kyoto-u.ac.jp/igrf/gggm/, respectively.

Acknowledgments

This work is carried out under the MI-PEARL program of IIG through grant-in-aid received from the Department of Science and Technology (DST), Govt. of India. The authors acknowledge the POLAR research group of IIG for the ICM data from Maitri, Antarctica. The authors thank Sodankylä Geophysical Observatory, University of Oulu, for the data of the Finnish pulsation magnetometer network. We acknowledge the Cluster FGM, instrument teams and the Cluster Science Archive. We acknowledge the substorm timing list identified by Newell and Gjerloev (2011a); Forsyth et al. (2015); Ohtani and Gjerloev (2020), the SMU and SML indices (Newell & Gjerloev, 2011b); and the SuperMAG collaboration (Gjerloev, 2012). The authors thank I.R. Mann, D.K. Milling and the rest of the CARISMA team for data. CARISMA is operated by the University of Alberta, funded by the Canadian Space Agency. The authors would like to acknowledge the International Space Science Institute (ISSI) in Bern for the opportunity it offered for constructive team discussions on this topic through the ISSI International Team project #522.

References

Allen, R. C., Zhang, J.-C., Kistler, L. M., Spence, H. E., Lin, R.-L., Klecker, B., ... Jordanova, V. K. (2015). A statistical study of EMIC waves observed by Cluster: 1. Wave properties. *J. Geophys. Res. Space Physics*, *120*, 5574-5592. doi: 10.1002/2015JA021333

Allen, R. C., Zhang, J.-C., Kistler, L. M., Spence, H. E., Lin, R.-L., Klecker, B., ... Jordanova, V. K. (2016). A statistical study of EMIC waves observed by Cluster: 2. Associated plasma conditions. *J. Geophys. Res. Space Physics*, *121*. doi: 10.1002/2016JA022541

Anderson, B. J., Erlandson, R. E., & Zanetti, L. J. (1992b). A statistical study of Pc 1-2 magnetic pulsations in the equatorial magnetosphere: 2. Wave properties. *J. Geophys. Res. Space Physics*, *97*, 3089-3101. doi: 10.1029/91JA02697

Anderson, B. J., & Hamilton, D. C. (1993). Electromagnetic ion cyclotron waves stimulated by modest magnetospheric compressions. *J. Geophys. Res. Space Physics*, *98*, 11369-11382. doi: 10.1029/93JA00605

Arnoldy, R. L., Lewis Jr., P. B., & Cahill Jr., L. J. (1979). Polarization of pc 1 and ipdp pulsations correlated with particle precipitation. *Journal of Geophysical Research: Space Physics*, *84*(A12), 7091-7098. Retrieved from https://agupubs.onlinelibrary.wiley.com/doi/abs/10.1029/JA084iA12p07091 doi: https://doi.org/10.1029/JA084iA12p07091

Balogh, A., Carr, C. M., Acuña, M. H., Dunlop, M. W., Beek, T. J., Brown, P., ... Schwingenschuh, K. (2001). The cluster magnetic field investigation: overview of in-flight performance and initial results. *Annales Geophysicae*, *19*(10/12), 1207–1217. Retrieved from https://angeo.copernicus.org/articles/19/1207/2001/ doi: 10.5194/angeo-19-1207-2001

Blake, J. B., Carranza, P. A., Claudepierre, S. G., Clemmons, J. H., Crain, W. R., Dotan, J., ... Zakrzewski, M. P. (2013). The Magnetic Electron Ion Spectrometer (MagEIS) instruments aboard the Radiation Belt Storm Probes (RBSP) spacecraft. *Space Science Reviews*, *179*, 1-4. doi: 10.1007/S11214-013-9991-8

Blum, L. W., Halford, A. J., Millan, R., Bonnell, J. W., Goldstein, J., Usanova, M., ...

Li, X. (2015). Observations of coincident EMIC wave activity and duskside energetic electron precipitation on 18–19 January 2013. *Geophys. Res. Lett.*, *42*, 5727–5735. doi: 10.1002/2015GL065245

Bortnik, J., Cutler, J. W., Dunson, C., & Bleier, T. E. (2007). An automatic wave detection algorithm applied to pc1 pulsations. *J. Geophys. Res.*, *112*(A04204). doi: 10.1029/2006JA011900

Cornwall, J. M., & Schulz, M. (1971). Electromagnetic ion-cyclotron instabilities in multicomponent magnetospheric plasmas. *J. Geophys. Res.*, *76*, 7791-7796. doi: 10.1029/JA076i031p07791

Engebretson, M. J., Peterson, W. K., Posch, J. L., Klatt, M. R., Anderson, B. J., Russell, C. T., ... Fukunishi, H. (2002). Observations of two types of pc 12 pulsations in the outer dayside magnetosphere. *Journal of Geophysical Research: Space Physics*, *107*(A12), SMP 20-1-SMP 20-20. Retrieved from https://agupubs.onlinelibrary.wiley.com/doi/abs/10.1029/2001JA000198 doi: https://doi.org/10.1029/2001JA000198

Engebretson, M. J., Posch, J. L., Wygant, J. R., Kletzing, C. A., Lessard, M. R., Huang, C.-L., ... Shiokawa, K. (2015). Van Allen probes, NOAA, GOES, and ground observations of an intense EMIC wave event extending over 12 h in magnetic local time. *J. Geophys. Res. Space Physics*, *120*, 5465–5488. doi: 10.1002/2015JA021227

Erlandson, R. E., & Ukhorskiy, A. J. (2001). Observations of electromagnetic ion cyclotron waves during geomagnetic storms: Wave occurrence and pitch angle scattering. *J. Geophys. Res.*, *106*(A3), 3883-3895. doi: 10.1029/2000JA000083

Escoubet, C. P., Fehringer, M., & Goldstein, M. (2001). Introductionthe cluster mission. *Annales Geophysicae*, *19*(10/12), 1197–1200. Retrieved from https://angeo.copernicus.org/articles/19/1197/2001/ doi: 10.5194/angeo-19-1197-2001

Forsyth, C., Rae, I. J., Coxon, J. C., Freeman, M. P., Jackman, C. M., Gjerloev, J., & Fazakerley, A. N. (2015). A new technique for determining substorm onsets and phases from indices of the electrojet (sophie). *Journal of Geophysical Research: Space Physics*, *120*(12), 10,592-10,606. Retrieved from https://agupubs.onlinelibrary.wiley.com/doi/abs/10.1002/2015JA021343 doi: https://doi.org/10.1002/2015JA021343

Fraser, B. J., & Nguyen, T. S. (2001). Is the plasmapause a preferred source region of electromagnetic ion cyclotron waves in the magnetosphere? *J. Atmos. Sol.-Terr. Phys.*, *63*(11), 1225-1247. doi: 10.1016/S1364-6826(00)00225-X

Funsten, H. O., Skoug, R. M., Guthrie, A. A., MacDonald, E. A., Baldonado, J. R., Harper, R. W., ... Chen, J. (2013). Helium, Oxygen, Proton, and Electron (HOPE) Mass Spectrometer for the Radiation Belt Storm Probes Mission. *Space Science Reviews*, *179*, 1-4. doi: 10.1007/s11214-013-9968-7

Gary, S. P. (1992). The mirror and ion cyclotron anisotropy instabilities. *Journal of Geophysical Research: Space Physics*, *97*(A6), 8519-8529. Retrieved from https://agupubs.onlinelibrary.wiley.com/doi/abs/10.1029/92JA00299 doi: https://doi.org/10.1029/92JA00299

Gjerloev, J. W. (2012). The supermag data processing technique. *Journal of Geophysical Research: Space Physics*, *117*(A9). Retrieved from https://agupubs.onlinelibrary.wiley.com/doi/abs/10.1029/2012JA017683 doi: https://doi.org/10.1029/2012JA017683

Grison, B., Santolk, O., Lukaevi, J., & Usanova, M. E. (2021). Occurrence of emic waves in the magnetosphere according to their distance to the magnetopause. *Geophysical Research Letters*, *48*(3), e2020GL090921. Retrieved from https://agupubs.onlinelibrary.wiley.com/doi/abs/10.1029/2020GL090921 (e2020GL090921 2020GL090921) doi: https://doi.org/10.1029/2020GL090921

Halford, A. J., Fraser, B. J., & Morley, S. K. (2010). EMIC wave activity during geomagnetic storm and nonstorm periods: CRRES results. *J. Geophys. Res.*, *115*. (A12248) doi: 10.1029/2010JA015716

Halford, A. J., Fraser, B. J., Morley, S. K., Elkington, S. R., & Chan, A. A. (2016). Depen-

dence of EMIC wave parameters during quiet, geomagnetic storm, and geomagnetic storm phase times. *J. Geophys. Res. Space Physics*, *121*, 6277–6291. (A12248) doi: 10.1002/2016JA022694

Henderson, M. (2024, July). *LANL Geosynchronous particle datafiles Limited Release Version 1.0.* Zenodo. Retrieved from `https://doi.org/10.5281/zenodo.12629463` doi: 10.5281/zenodo.12629463

Johnson, J. R., & Cheng, C. Z. (1999). Can ion cyclotron waves propagate to the ground? *Geophysical Research Letters*, *26*(6), 671-674. Retrieved from `https://agupubs.onlinelibrary.wiley.com/doi/abs/10.1029/1999GL900074` doi: https://doi.org/10.1029/1999GL900074

Johnstone, A. D., Alsop, C., Burge, S., Carter, P. J., Coates, A. J., Coker, A. J., ... Woodliffe, R. D. (1997). Peace: a plasma electron and current experiment. *Space Science Reviews*, *79*, 351-398. Retrieved from `https://ui.adsabs.harvard.edu/abs/1997SSRv...79..351J` doi: 10.1023/A:1004938001388

Jordanova, V. K., Albert, J., & Miyoshi, Y. (2008). Relativistic electron precipitation by EMIC waves from self-consistent global simulations. *J. Geophys. Res.*, *113*. (A00A10) doi: 10.1029/2008JA013239

Keika, K., Takahashi, K., Ukhorskiy, A. Y., & Miyoshi, Y. (2013). Global characteristics of electromagnetic ion cyclotron waves: Occurrence rate and its storm dependence. *J. Geophys. Res. Space Physics*, *118*, 4135-4150. doi: 10.1002/jgra.50385

Kennel, C. F., & Petschek, H. E. (1966). Limit on stably trapped particle fluxes. *J. Geophys. Res.*, *71*, 1-28. doi: 10.1029/JZ071i001p00001

Kletzing, C. A., Kurth, W. S., Acuna, M., MacDowall, R. J., Torbert, R. B., Averkamp, T., ... Tyler, J. (2013). The Electric and Magnetic Field Instrument Suite and Integrated Science (EMFISIS) on RBSP. *Space Sci. Rev.*, *179*, 127–181. doi: 10.1007/s11214-013-9993-6

Kozyra, J. U., Cravens, T. E., Nagy, A. F., Fontheim, E. G., & Ong, R. S. B. (1984). Effects of energetic heavy ions on electromagnetic ion cyclotron wave generation in the plasma-pause region. *J. Geophys. Res.*, *89*(A4), 2217-2233. doi: 10.1029/JA089iA04p02217

Loto'aniu, T. M., Fraser, B. J., & Waters, C. L. (2005). Propagation of electromagnetic ion cyclotron wave energy in the magnetosphere. *J. Geophys. Res.*, *110*. (A07214) doi: 10.1029/2004JA010816

Mann, I. R., Milling, D. K., Rae, I. J., Ozeke, L. G., Kale, A., Kale, Z. C., ... Singer, H. J. (2008). The upgraded CARISMA magnetometer array in the THEMIS era. *Space Science Reviews*, *141*, 413-451. doi: 10.1007/s11214-008-9457-6

Mauk, B. H., Fox, N. J., Kanekal, S. G., Kessel, R. L., Sibeck, D. G., & Ukhorskiy. (2013). Science objectives and rationale for the radiation belt storm probes mission. *Space Science Reviews*, *179*, 3-27. Retrieved from `https://doi.org/10.1007/s11214-012-9908-y` doi: https://doi.org/10.1007/s11214-012-9908-y

McCollough, J. P., Elkington, S. R., & Baker, D. N. (2012). The role of shabansky orbits in compression-related electromagnetic ion cyclotron wave growth. *J. Geophys. Res.*, *117*(A01208). doi: 10.1029/2011JA016948

Min, K., Lee, J., Keika, K., & Li, W. (2012). Global distribution of EMIC waves derived from THEMIS observations. *J. Geophys. Res.*, *117*. (A05219) doi: 10.1029/2012JA017515

Mitchell, D. G., Lanzerotti, L. J., Kim, C. K., Stokes, M., Ho, G., Cooper, S., ... Kerem, S. (2013). Radiation belt storm probes ion composition experiment (rbspice). *Space Science Reviews*, *179*, 263-308. Retrieved from `https://doi.org/10.1007/s11214-013-9965-x` doi: 10.1007/s11214-013-9965-x

Newell, P. T., & Gjerloev, J. W. (2011a). Evaluation of SuperMAG auroral electrojet indices as indicators of substorms and auroral power. *J. Geophys. Res.*, *116*. (A12211) doi: 10.1029/2011JA016779

Newell, P. T., & Gjerloev, J. W. (2011b). Substorm and magnetosphere characteristic scales inferred from the supermag auroral electrojet indices. *Journal of Geophysical Research: Space Physics*, *116*(A12). Retrieved from `https://agupubs.onlinelibrary.wiley.com/doi/abs/10.1029/2011JA016936` doi: https://doi

.org/10.1029/2011JA016936

Noh, S.-J., Lee, D.-Y., Choi, C.-R., Kim, H., & Skoug, R. (2018). Test of ion cyclotron resonance instability using proton distributions obtained from van allen probe-a observations. *Journal of Geophysical Research: Space Physics*, *123*(8), 6591-6610. Retrieved from https://agupubs.onlinelibrary.wiley.com/doi/abs/10.1029/2018JA025385 doi: https://doi.org/10.1029/2018JA025385

Ohtani, S., & Gjerloev, J. W. (2020). Is the substorm current wedge an ensemble of wedgelets?: Revisit to midlatitude positive bays. *Journal of Geophysical Research: Space Physics*, *125*(9), e2020JA027902. Retrieved from https://agupubs.onlinelibrary.wiley.com/doi/abs/10.1029/2020JA027902 (e2020JA027902 2020JA027902) doi: https://doi.org/10.1029/2020JA027902

Olson, J. V., & Lee, L. C. (1983). Pc1 wave generation by sudden impulses. *Planet. Space Sci.*, *31*(3), 295-297. doi: 10.1016/0032-0633(83)90079-X

Park, J.-S., Kim, K.-H., Shiokawa, K., Lee, D.-H., Lee, E., Kwon, H.-J., ... Jee, G. (2016). Emic waves observed at geosynchronous orbit under quiet geomagnetic conditions (kp$\leq$ 1). *Journal of Geophysical Research: Space Physics*, *121*(2), 1377-1390. Retrieved from https://agupubs.onlinelibrary.wiley.com/doi/abs/10.1002/2015JA021968 doi: https://doi.org/10.1002/2015JA021968

Rauch, J. L., & Roux, A. (1982). Ray tracing of ULF waves in a multicomponent magnetospheric plasma: Consequences for the generation mechanism of ion cyclotron waves. *J. Geophys. Res.*, *87*(A10), 8191-8198. doi: 10.1029/JA087iA10p08191

Reeves, G., Belian, R., Cayton, T., Christensen, R., Henderson, M., & McLachlan, P. (1996, October). Los Alamos space weather data products: on line and on time. In E. Rolfe & B. Kaldeich (Eds.), *International conference on substorms* (Vol. 389, p. 689).

Rème, H., Aoustin, C., Bosqued, J. M., Dandouras, I., Lavraud, B., Sauvaud, J. A., ... Sonnerup, B. (2001). First multispacecraft ion measurements in and near the earths magnetosphere with the identical cluster ion spectrometry (cis) experiment. *Annales Geophysicae*, *19*(10/12), 1303–1354. Retrieved from https://angeo.copernicus.org/articles/19/1303/2001/ doi: 10.5194/angeo-19-1303-2001

Remya, B. (2024a, November). *Emic wave event list from van allen probes.* Zenodo. Retrieved from https://doi.org/10.5281/zenodo.14195258 doi: 10.5281/zenodo.14195258

Remya, B. (2024b, August). *Icm data for maitri, antarctica.* Zenodo. Retrieved from https://doi.org/10.5281/zenodo.13149317 doi: 10.5281/zenodo.13149317

Remya, B., Halford, A. J., Sibeck, D. G., Murphy, K. R., & Fok, M.-C. (2023). Understanding quiet and storm time emic wavesvan allen probes results. *Journal of Geophysical Research: Space Physics*, *128*(8), e2023JA031712. Retrieved from https://agupubs.onlinelibrary.wiley.com/doi/abs/10.1029/2023JA031712 (e2023JA031712 2023JA031712) doi: https://doi.org/10.1029/2023JA031712

Remya, B., Sibeck, D. G., Halford, A. J., Murphy, K. R., Reeves, G. D., Singer, H. J., ... Thaller, S. A. (2018). Ion injection triggered emic waves in the earth's magnetosphere. *J. Geophys. Res. Space Physics*, *123*. doi: 10.1029/2018JA025354

Remya, B., Sibeck, D. G., Ruohoniemi, J. M., Kunduri, B., Halford, A. J., Reeves, G. D., & Reddy, R. V. (2020). Association between emic wave occurrence and enhanced convection periods during ion injections. *Geophys. Res. Lett.*, *47*(e2019GL085676). doi: 10.1029/2019GL085676

Remya, B., Tsurutani, B. T., Reddy, R. V., Lakhina, G. S., & Hajra, R. (2015). Electromagnetic cyclotron waves in the dayside subsolar outer magnetosphere generated by enhanced solar wind pressure: EMIC wave coherency. *J. Geophys. Res. Space Physics*, *120*. doi: 10.1002/2015JA021327

Shiokawa, K., Nomura, R., Sakaguchi, K., Otsuka, Y., Hamaguchi, Y., Satoh, M., ... Connors, M. (2010). The stel induction magnetometer network for observation of high-frequency geomagnetic pulsations. *Earth, Planets and Space*, *62*(6), 517-524. Retrieved from https://doi.org/10.5047/eps.2010.05.003 doi: 10.5047/eps.2010.05.003

Singer, H., Matheson, L., Grubb, R., Newman, A., & Bouwer, D. (1996, October). Monitoring space weather with the GOES magnetometers. In E. Washwell (Ed.), *Goes-8 and beyond* (Vol. 2812, p. 299-308). doi: 10.1117/12.254077

Spence, H., Reeves, G., Baker, D., Blake, J., Bolton, M., Bourdarie, S., ... Thorne, R. (2013). Science goals and overview of the Radiation Belt Storm Probes (RBSP) Energetic particle, Composition, and Thermal plasma (ECT) suite on NASA's Van Allen Probes Mission. *Space Sci. Rev.*, *179*, 311–336. doi: 10.1007/s11214-013-0007-5

Thorne, R. M., & Kennel, C. F. (1971). Relativistic electron precipitation during magnetic storm main phase. *J. Geophys. Res.*, *76*(19), 4446-4453. doi: 10.1029/JA076i019p04446

Tsyganenko, N. (1989). A magnetospheric magnetic field model with a warped tail current sheet. *Planetary and Space Science*, *37*(1), 5-20. Retrieved from `https://www.sciencedirect.com/science/article/pii/0032063389900664` doi: https://doi.org/10.1016/0032-0633(89)90066-4

Usanova, M. E., Mann, I. R., Bortnik, J., Shao, L., & Angelopoulos, V. (2012). THEMIS observations of electromagnetic ion cyclotron wave occurrence - Dependence on AE, SYMH, and solar wind dynamic pressure. *J. Geophys. Res. Space Physics*, *117*. (A10218) doi: 10.1029/2012JA018049

Usanova, M. E., Mann, I. R., Rae, I. J., Kale, Z. C., Angelopoulos, V., Bonnell, J. W., ... Singer, H. J. (2008). Multipoint observations of magnetospheric compression-related emic pc1 waves by themis and carisma. *Geophys. Res. Lett.*, *35*(L17S25). doi: 10.1029/2008GL034458

Vasyliunas, V. M. (1975). An overview of magnetospheric dynamics. *in Magnetospheric Particles and Fields*, 99.

Wang, D., Yuan, Z., Yu, X., Deng, X., Zhou, M., Huang, S., ... Wygant, J. R. (2015). Statistical characteristics of emic waves: Van allen probe observations. *J. Geophys. Res. Space Physics*, *120*, 4400-4408. doi: 10.1002/2015JA021089

Weimer, D. R. (2005). Improved ionospheric electrodynamic models and application to calculating joule heating rates. *Journal of Geophysical Research: Space Physics*, *110*(A5). Retrieved from `https://agupubs.onlinelibrary.wiley.com/doi/abs/10.1029/2004JA010884` doi: https://doi.org/10.1029/2004JA010884

Young, D. T., Perraut, S., Roux, A., de Villedary, C., Gendrin, R., Korth, A., ... Jones, D. (1981). Wave-particle interactions near Ω_{He^+} observed on GEOS 1 and 2: 1. Propagation of ion cyclotron waves in Ω_{He^+}-rich plasma. *J. Geophys. Res.*, *86*(A8), 6755-6772. doi: 10.1029/JA086iA08p06755